

All germanium-based double absorption layer perovskite solar cell based on SCAPS-1D analysis



Lijing Su^a, Pengfei Sun^a, Yaxin Zhou^a, Xin Li^a, Sihan Nie^a, Yang Gao^{a,b,*}

^a School of Electronic Engineering, Heilongjiang University, Heilongjiang, 150080, China

^b Heilongjiang Provincial Key Laboratory of metamaterials physics and device, Heilongjiang University, Heilongjiang, 150080, China

ARTICLE INFO

Keywords:
SCAPS-1D
Solar cell
Double absorber layer
Ge-based perovskite

ABSTRACT

In this study, we focus on optimizing the structure of perovskite solar cells (PSCs) comprising a single absorption layer of FTO/n-CsGeI₃/MAGeI₃/p-CsGeI₃/Pt. Subsequently, a novel double absorption layer structure based on FTO/n-CsGeI₃/MAGeI₃/CsGeI₃/p-CsGeI₃/Pt PSCs is proposed. We have designed high-performance devices by selectively integrating CsGeI₃ (low bandgap of 1.6 eV) and MAGeI₃ (high bandgap of 1.9 eV) materials. Previous research has demonstrated that incorporating a layered absorber with low and high bandgap layers can substantially improve the performance of PSCs. Herein, we modelled and analyzed the performance of PSCs using the SCAPS-1D simulator. Through simulation of the double absorption layer PSCs, we achieve optimal device configurations, yielding a PCE of 26.85 %, a J_{sc} of 23.39 mA/cm², a FF of 88.19 %, and a Voc of 1.30V.

1. Introduction

Solar energy stands out as the most promising avenue for ameliorating biosphere challenges and addressing environmental issues [1–5]. New photovoltaic technologies, in particular the third-generation photovoltaic material perovskite, is one of the most efficient solar cell materials. In the past decade, there has been a notable progress in the efficiency of third-generation solar cells that use organic-inorganic halogen-based elements. In 2022, there was a significant 25.7 % improvement in photoelectric conversion efficiency (PCE) [6–11]. Hybrid perovskite and Pb-based perovskite are two of the most extensively researched materials due to their unique photovoltaic properties, which result in enhanced PCE [12–15]. However, the toxicity of Pb poses serious health and environmental risks. As a solution to these problems, Pb-free perovskite solar cells have been developed, with some researchers turning to alternatives like Sn and Ge due to their chemical similarity to lead without the associated health hazards. Sn, in particular, is abundant in nature and has minimal adverse effects on humans and the environment [16]. Despite the narrower bandgap and superior light-absorbing properties of Sn-based perovskites compared to Pb-based ones [17], their susceptibility to oxidation from Sn²⁺ to Sn⁴⁺ undermines the structural stability and consequently, the PCE is lower [18,19]. The Ge-based perovskite has been identified as a promising absorbent layer for perovskite solar cells due to its wide bandgap [20,

21]. In 2015, Krishnamoorthy et al. demonstrated remarkable stability at high temperatures in their PSCs, using Ge-based perovskite as the absorption layer for solar cells [22]. The complexity and economic impact associated with manufacturing double-absorbing layer structures compared to single-absorbing layer structures may hinder their feasibility for mass production. Ge-based solar cells have shown significant benefits in terms of material availability and environmental compatibility. Nevertheless, they are still faced with the need to improve the PCE and maintain structural long-term stability. The upcoming survey work must overcome these obstacles to facilitate the realization of high-performance and ecologically sound photovoltaic technologies.

This study proposes the replacement of both the electron transport layer (ETL) and hole transport layer (HTL) in the original structure with CsGeI₃. By constructing n-CsGeI₃ and p-CsGeI₃, efficient carrier transport can be achieved. This improves environmental protection and the efficiency of transportation. SCAPS-1D (Solar cell capacitor simulator -1D) is used to construct this new type of photovoltaic device. The optimum process conditions are obtained by optimizing the parameters of band gap, absorber thickness and bulk defect density. The findings indicate that this approach effectively reduces the recombination probability of the photogenerated carrier, consequently enhancing the PCE of the device. Building upon these results, this study delves into the investigation of double absorption layer based on all-Ge based cell.

* Corresponding author. School of Electronic Engineering, Heilongjiang University, Heilongjiang, 150080, China.

E-mail address: gao_y_hit@163.com (Y. Gao).

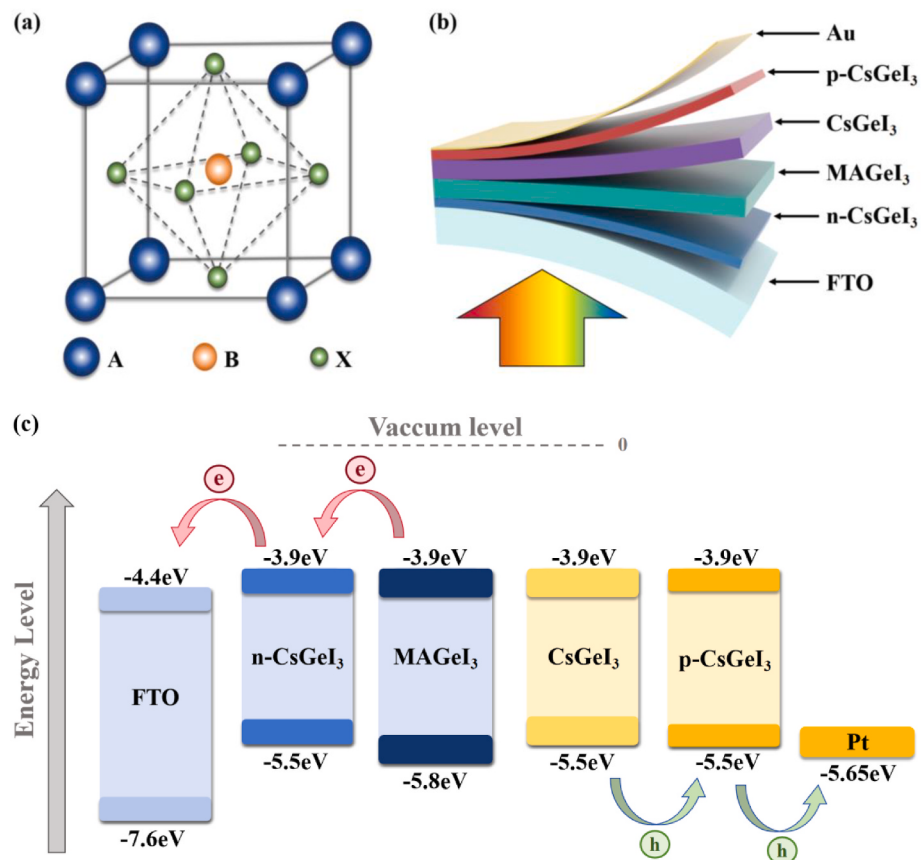


Fig. 1. (a) Molecular structure diagram of perovskite; (b) Structure of solar cell; (c) Energy band distribution of different materials.

2. Simulation and material parameters

At present, several simulation software are extensively employed in the research of solar cells, such as SETFOS, SCAPS, SILVACO, COMSOL and ATLAS [23–28]. SCAPS-1D, a unidimensional solar cell simulation software suite with a focus on the architectural intricacies of CuInSe₂ and CdTe-based photovoltaic cells. Its applications have since been expanded to encompass the design and computational simulation of silicon-based and efficacious Pb-free heterostructured perovskite photovoltaic devices. All simulation calculations in this research are conducted using SCAPS-1D version 3.3.10. In SCAPS-1D calculations, the Poisson and continuity equations are utilised for the solution, as shown below [29]:

$$-\frac{\partial}{\partial x} \left(-\epsilon(x) \frac{\partial V}{\partial x} \right) = q [p(x) - n(x) + N_D^-(x) - N_A^-(x) + p_t(x) - n_t(x)] \quad (1)$$

$$\frac{\partial n}{\partial t} = \frac{1}{q} \frac{\partial J_n}{\partial x} + G_n - R_n \quad (2)$$

$$\frac{\partial p}{\partial t} = \frac{1}{q} \frac{\partial J_p}{\partial x} + G_p - R_p \quad (3)$$

In this equation, q denotes charge, ϵ stands for dielectric permittivity, V represents electrostatic potential energy, $p(x)/n(x)$ signifies the concentration of free holes/electrons, $N_D^+(x)/N_A^+(x)$ represents the concentration of ionized donors/acceptors, $p_t(x)/n_t(x)$ denotes the holes/electrons trap density, J_p/J_n signifies the holes/electrons current density, G_p/G_n indicates the generation rate of holes/electrons, R_p/R_n denotes the holes/electrons recombination rate. From these equations, four photovoltaic parameters are derived: PCE, short-circuit current density (J_{sc}), fill factor (FF), and open-circuit voltage (V_{oc}). These parameters are interconnected as described in Eqs. (4) and (5) [30].

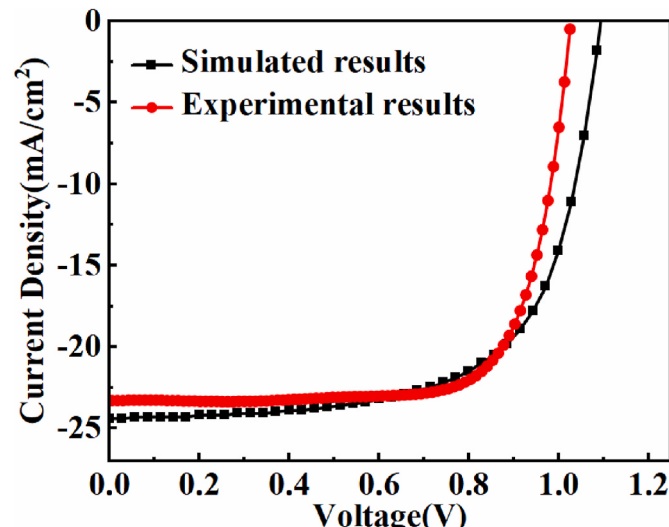


Fig. 2. J-V characteristics of simulation and measurements.

$$PCE = \frac{J_{sc} \times V_{oc} \times FF}{P_{int}} \quad (4)$$

$$FF = \frac{V_{max} \times J_{max}}{V_{oc} J_{sc}} \quad (5)$$

PSCs have become a hotspot for research due to their excellent photovoltaic properties, of which the typical structure is shown in Fig. 1 (a), usually has the chemical formula ABX₃, in which the A-position is a

Table 1
Material parameters used in simulation.

Material properties	FTO	n-CsGeI ₃	MAGeI ₃	CsGeI ₃	p-CsGeI ₃
Thickness (nm)	500	20	400	400	200
E_g (eV)	3.5	1.8	1.9	1.6	1.8
X (eV)	4.0	4.0	3.9	3.9	4.0
ϵ_r	9.0	18.0	10.0	6.5	18.0
N_D (cm ⁻³)	1.0 × 10 ¹⁹	2.0 × 10 ¹⁹	0	0	0
N_A (cm ⁻³)	0	0	1.0 × 10 ¹⁴	1.0 × 10 ¹⁴	2.0 × 10 ¹⁶
N_c (cm ⁻³)	2.2 × 10 ¹⁸	1.0 × 10 ¹⁸	1.0 × 10 ¹⁶	1.0 × 10 ¹⁸	1.0 × 10 ¹⁸
N_v (cm ⁻³)	1.8 × 10 ¹⁹	1.0 × 10 ¹⁹	1.0 × 10 ¹⁵	1.0 × 10 ¹⁸	1.0 × 10 ¹⁹
M_n (cm ² /Vs) ⁻¹	20.0	20.0	1.62 × 10 ⁵	50.0	20.0
M_p (cm ² /Vs) ⁻¹	10.0	20.0	1.01 × 10 ⁵	50.0	20.0
N_T (cm ⁻³)	1.0 × 10 ¹⁵	1.0 × 10 ¹⁵	1.0 × 10 ¹⁴	1.0 × 10 ¹⁴	1.0 × 10 ¹⁵
Reference	[32]	[33]	[32]	[34]	[33]

Table 2
Nomenclature.

Full name	Abbreviation
acceptor doping concentration	N_A
bandgap	E_g
bulk defect concentration	N_T
conduction band effective density of states	N_C
donor concentration	N_D
electron affinity	χ
electron mobility	M_n
hole mobility	M_p
quasi-Fermi level of the electron	F_n
quasi-Fermi level of the hole	F_p
relative permittivity	ϵ_r
valence band effective density of states	N_V

cation with a larger radius, the B-position is a cation with a smaller radius, and X is a halogen. The structure of the perovskite solar cell mentioned in this article is shown in Fig. 1(b) and (c). The whole structure of the cell is: the front electrode is used as the doped tin fluoride oxide (FTO); ETL as n-CsGeI₃; Light absorbing materials as MAGeI₃ and CsGeI₃; HTL as p-CsGeI₃; The back electrode is platinum (Pt).

Theoretical calculation simulation was carried out on the MaPbI_3 -based photovoltaic cell, which has a hierarchical structure of FTO/TiO₂/C₆₀/MAPbI₃/Spiro-OMeTAD/Au [31]. The synthetic J-V characteristics obtained by SCAPS simulation platform are shown in Fig. 2. A visual analysis of the graph shows that the simulation results are consistent with those reported in existing academic publications.

The initial simulation employs the specified structure of PSCs. Input parameters for the initial structure are tabulated in Table 1, sourced from theory considerations and previous references. The full names of the nomenclature referred to in Table 1 are shown in Table 2. Additionally, this paper uses that both the electron/hole thermal velocities are 10^7 cm/s .

Assume a constant illumination of 300 K, AM 1.5G, and 1000 W/m². The work function of the back electrode Pt is 5.65 eV. The doping concentration of MAGeI₃ and CsGeI₃ is fixed at 10^{14} cm^{-3} . In this study, some material parameters will be discussed and optimised. From the provided data, the following photovoltaic parameters are obtained: $V_{oc} = 1.23 \text{ V}$, $J_{sc} = 21.64 \text{ mA/cm}^2$, FF = 87.90 %, PCE = 23.40 %.

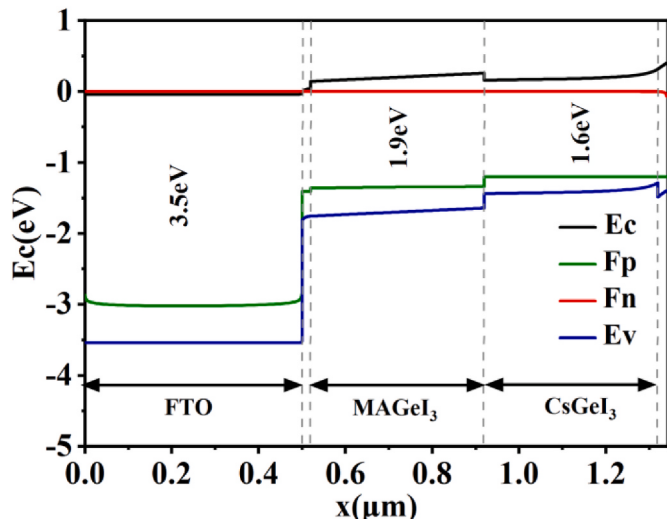


Fig. 3. Band diagram of materials in contact.

3. Simulation and result analysis

Fig. 3 shows the energy band diagram of perovskite solar cells in contact with each other under specific parameters. Fermi levels autonomously regulate the overall thermal equilibrium. However, when subjected to light excitation, the carriers in the absorber will lose their ability to maintain this equilibrium. The built-in voltage (V_{bi}) depends on the distance between the quasi-Fermi level of the electron (F_n) and the hole (F_p) and the energy gap, which can be expressed as $qV_{bi} = E_g - (F_n + F_p)$ [35]. Under the equilibrium state where the applied voltage $V = V_{bi}$, photogenerated carriers are effectively accumulated in the contact layer. Conversely, when $V > V_{bi}$, the electric field between the absorption layer and the transfer layer impedes charge collection, diminishing both PCE and FF [36]. Conduction band offset (CBO) denotes the disparity in the conduction band (CB) levels between different layers [37]. If there is a spike at the ETL/absorption interface, the CB bottom of the ETL is exactly higher than the CB bottom of the absorption layer, hindering electron migration. Under negative CBO conditions, if the minimum CB in perovskite is greater than ETL, a 'cliff' forms between the electrons and the light absorbing layer, allowing a smooth flow of electrons to the back electrode [38]. Similarly, for the hole flow to the positive electrode, the maximum valence band (VB) value of HTL should be greater than that of perovskite.

In PSCs, the thickness of perovskite directly determines the absorption capacity of sunlight and the transmission capacity of photo-generated carriers, so the appropriate layer thickness is the key factor to determine its performance. On this basis, this study delves into the thickness of the double-layer light-absorbing layer and its influence on cell efficiency. Fig. 4 shows the variation in photoelectric characteristic parameters of the designed cell at different thicknesses of MAGeI₃ and CsGeI₃.

The absorption layers range in thickness from 100 to 1000 nm. Moreover, the PCE exhibits an increasing trend with the thickness of the perovskite absorbing layer, stabilizing around 700 nm. At thinner thicknesses, redirection of the incident light leads to a reduction in photogenerated electron-hole pairs, consequently diminishing the PCE of the device. Additionally, Fig. 4(a) shows that the wide absorbent layer has a significant impact on Voc. Increasing the thickness of the wide band absorber layer from 100 nm to 700 nm results in a significant increase in the Voc. As the thickness of CsGeI₃ increases, it enhances the cell's photon absorption and electron generation, improving the Jsc and PCE. However, a continuous increase in thickness can also lead to a rise in defects within the perovskite material, which may intensify carrier recombination. This could cause the photovoltaic parameters to stabilize

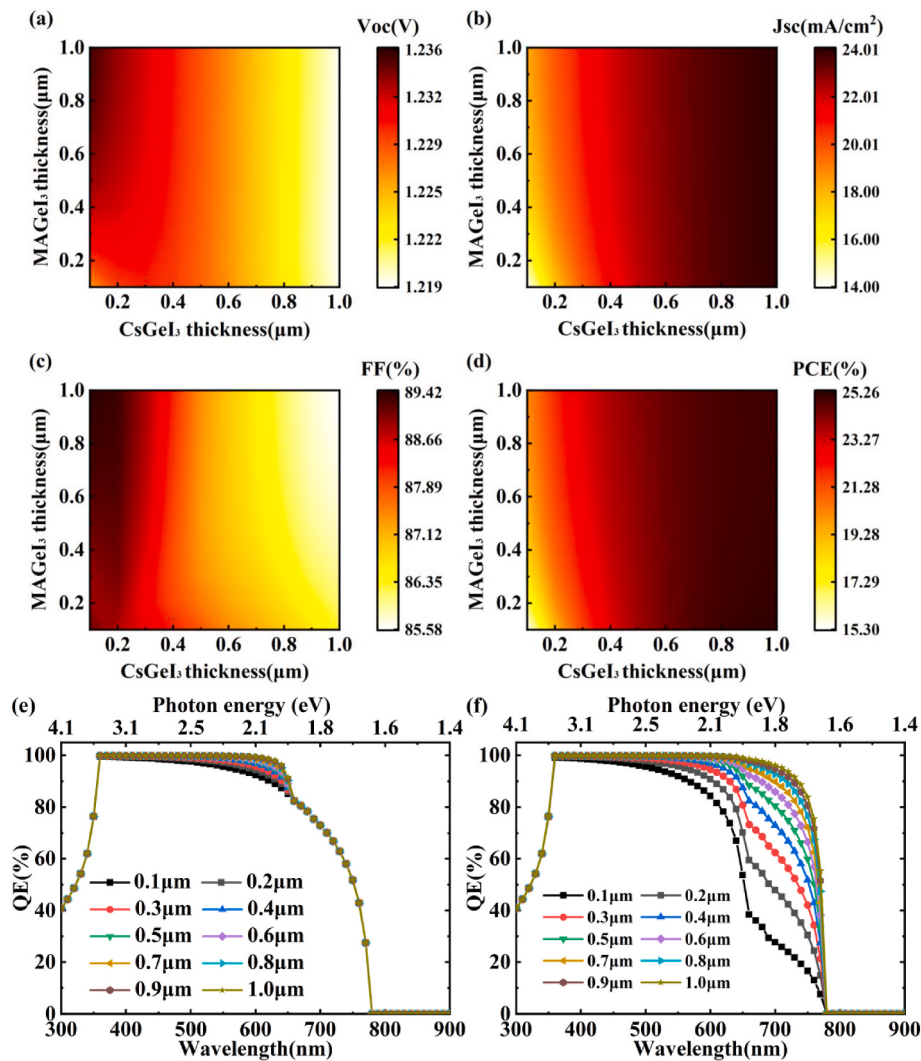


Fig. 4. (a-d) Influence of absorption layer thickness on V_{oc} , J_{sc} , FF and PCE; (e) The influence of MAGel_3 thickness on QE; (f) The influence of CsGeI_3 thickness on QE.

or even decline, particularly affecting the V_{oc} and FF. However, within the 700–1000 nm range, the V_{oc} remains relatively constant. CsGeI_3 and MAGel_3 with a 700 nm light absorbing layer are selected for this study based on the above criteria.

By adjusting the thickness of one of the absorber layers while fixing the other, one can obtain the quantum efficiency (QE) curve of the cell, as illustrated in Fig. 4(e) and (f). The simulated findings indicate that simultaneously modifying the thicknesses of both absorber layers exerts a beneficial influence on the QE of the cell. Notably, augmenting the thickness of the absorber layer diminishes the loss of solar irradiance, augmenting the utilization of electron-hole pairs, and consequently enhancing the overall performance of the cell.

The defects mentioned in this paper are mainly neutral defects. A “neutral” defect is an idealization of a defect that contributes to the Shockley-Read-Hall composite, but does not contribute to the space charge. The influence of altering the bulk defect density in the absorbing layer on key photovoltaic metrics of the cell is presented as follows. Fig. 5(a) and (b) exhibit how the output characteristics of the device respond as the bulk defect density of the $\text{MAGel}_3/\text{CsGeI}_3$ perovskite absorbing layer varies from 1×10^{13} to $1 \times 10^{20} \text{ cm}^{-3}$. As evident in Fig. 5(c) and (d), all four photovoltaic parameters exhibit a decline as the defect density rises. Notably, the PCE metric undergoes a substantial drop from 25.00 % to 18.14 % when the defect density of MAGel_3 attains 10^{19} cm^{-3} . With the increase of N_t , the carrier recombination rate in

double-absorbing layer photovoltaic devices increases significantly. This phenomenon indicates that the surge of N_t reduces the carrier lifetime and diffusion length, which ultimately leads to the reduction of photo-induced carrier collection efficiency and the degradation of carrier mass [39]. As shown in Fig. 5(d), when the defect density of perovskite material increases, FF of solar cells decreases first and then increases. This may be due to a combination of factors. In the stage of low defect density, the defects mainly affect the carrier transport and recombination process as the charge trapping center and scattering center. In the stage with high defect density, the effective carrier transmission and collection may be promoted through the trap saturation effect mechanism [40].

Simultaneously, the figure demonstrates the variation in QE under different absorption layer defect conditions, as depicted in Fig. 6. As illustrated in Fig. 6(b), an increase in CsGeI_3 defects results in a decrease in overall photon absorption by the device. This decline is particularly pronounced when the defect exceeds 10^{19} cm^{-3} , which aligns with the information presented in Fig. 6.

With different defects.

As depicted in Fig. 7, there is a discernible downward trend in the overall device performance in conjunction with the increased thickness of the ETL. The photovoltaic performance of the device is more significantly influenced by variations in the thickness of the HTL. Specifically, increasing the HTL thickness from 20 nm to 200 nm, leads to a gradual

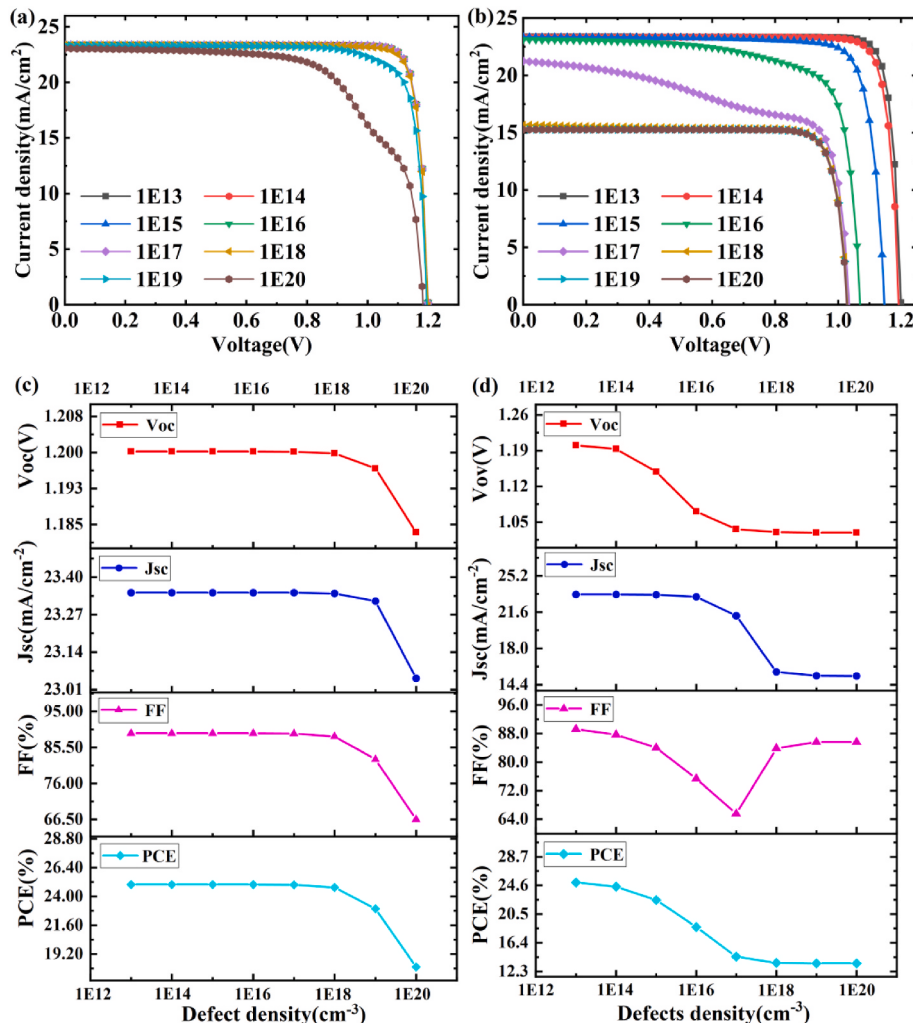


Fig. 5. (a) J-V curves of MAGeI₃ with different defects; (b) J-V curves of CsGeI₃ with different defects; (c) Influence of photovoltaic parameters under different defects of MAGeI₃; (d) Influence of photovoltaic parameters under different defects of CsGeI₃.

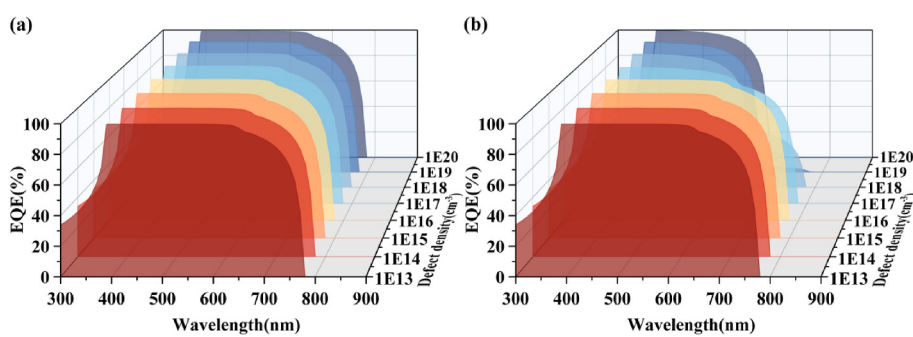


Fig. 6. (a) QE curves of MAGeI₃ with different defects; (b) QE curves of CsGeI₃.

increase in the Voc, accompanied by a gradual decrease in the FF. The optimal performance is achieved when the HTL is 200 nm. Similarly, alterations in the ETL thickness from 10 nm to 100 nm significantly impact the Jsc and the PCE in the photovoltaic parameters of the cell, as shown in Fig. 7(b) and (d). Increasing the HTL thickness facilitates the efficient extraction of photogenerated holes and mitigates electron recombination, thereby effectively suppressing charge recombination processes. This, in turn, leads to a substantial enhancement in the PCE of solar cell [41]. It can be inferred that a thickness of 20 nm is the most suitable value for the ETL.

The device's photoelectric properties are sensitive to operating temperature, and our study focuses on exploring this relationship within a temperature range spanning from 300 K to 400 K. As shown in Fig. 8, the reverse saturation current increases significantly with increasing ambient temperature, resulting in lower Voc and PCE of the cell. The increase in temperature stimulates the thermal motion of particles within the cell, which in turn accelerates the rate of electron-hole pair formation, ultimately leading to an increase in Jsc. Despite the increase in Jsc, the FF of the cell decreases with increasing temperature, which is a detrimental effect that can be attributed to several factors: Firstly, at

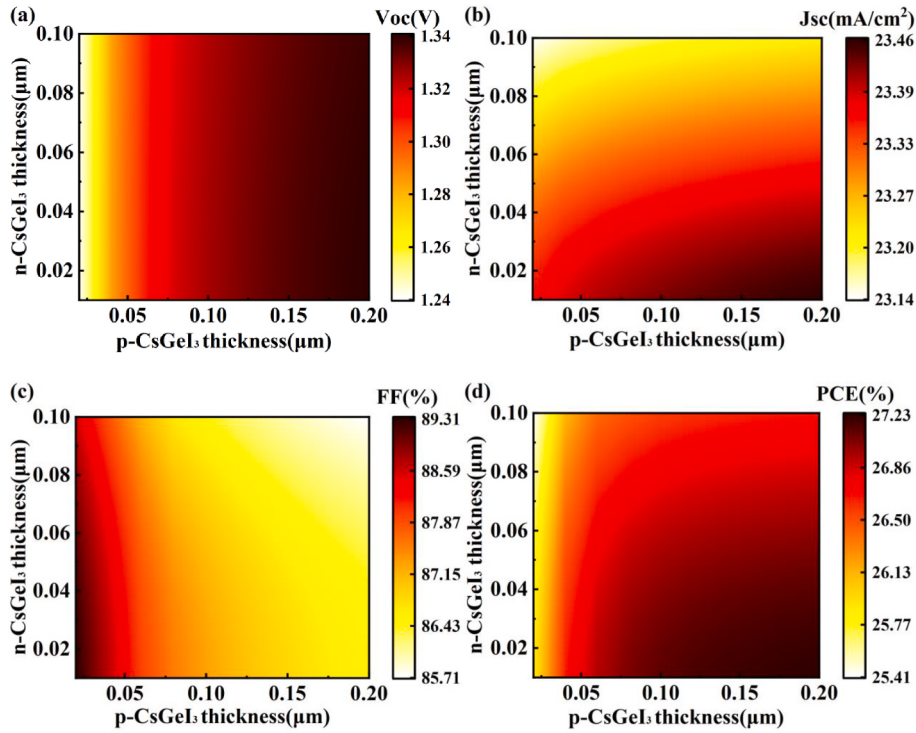


Fig. 7. Influence of transport layer thickness on: (a) Voc; (b) Jsc; (c) FF, and (d) PCE.

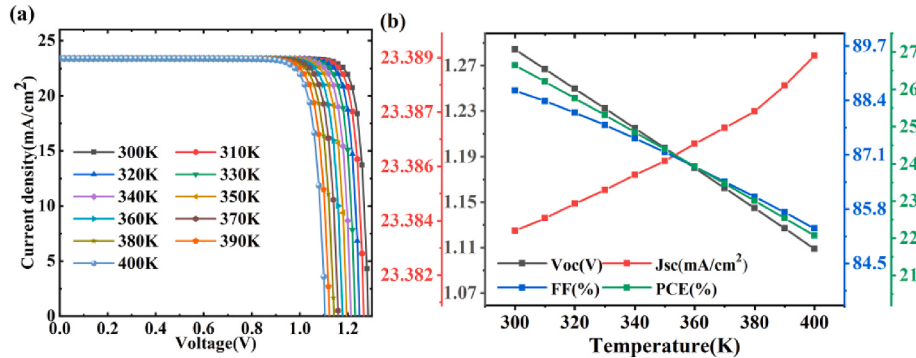


Fig. 8. (a) J-V curves of solar cells at different temperatures; (b) Influence of different temperatures on photovoltaic parameters of solar cells.

high temperatures, the increase in the defect density in the cell material increases scattering and trapping during charge transport; secondly, thermal stresses induced changes in the internal microstructure of the material, which impedes the efficient migration of carriers; and lastly,

with the increase in temperature, the acceleration of the recombination rate reduces the number of carriers available for photocurrent generation [42].

Solar cells contain series resistance, shunt resistance, and other

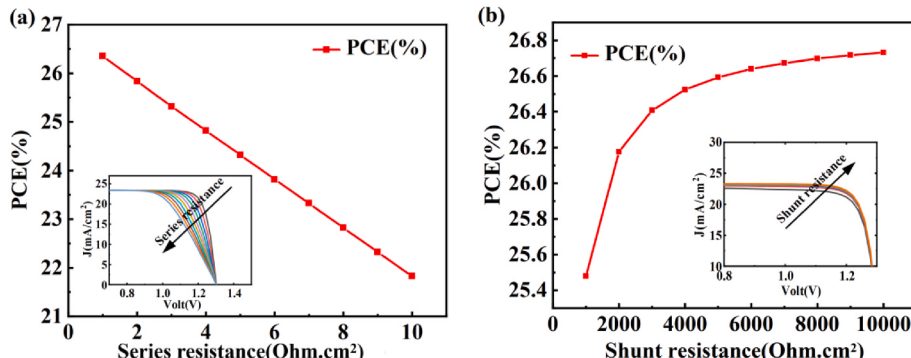


Fig. 9. (a) J-V curves of at different temperatures; (b) Influence of different temperatures on photovoltaic parameters of solar cells.

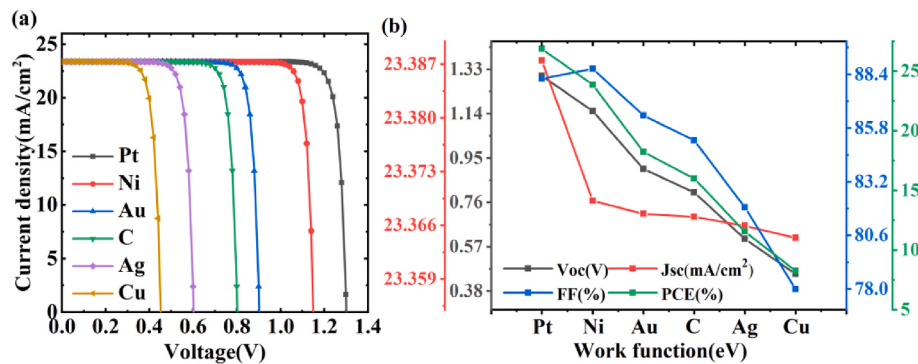


Fig. 10. (a) J-V curve with different back electrode; (b) Effect of different back electrode on photovoltaic characteristics of solar cells.

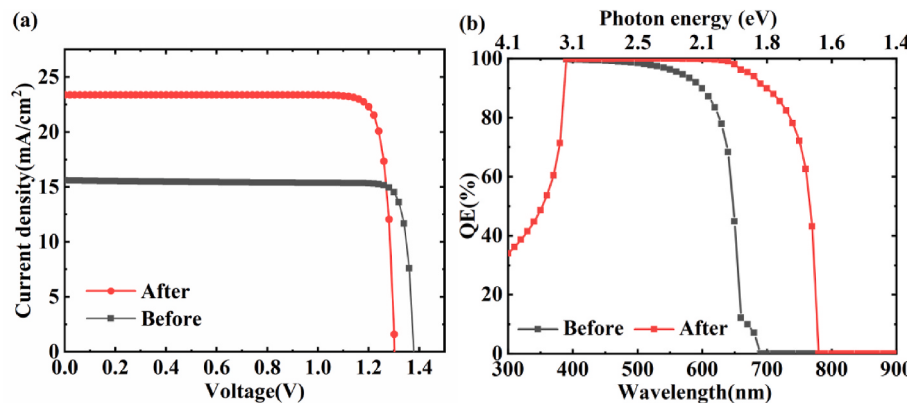


Fig. 11. (a) J-V curves before and after optimization; (b) Quantum efficiency curves before and after optimization.

parasitic resistance, all of which significantly impact the cell's PCE. One important factor contributing to series resistance is front and back electrode resistance. These resistances can significantly affect the PCE of the cell. Additionally, an increase in interlayer resistance can also lead to an increase in the series resistance of the cell. It is important to note that series resistance is an inherent characteristic of solar cells and cannot be completely eliminated. To achieve high efficiency solar cells, it is crucial to have both low series resistance and large shunt resistance. To improve device performance, we deliberately escalated the series resistance, elevating it from 1 Ohm.cm² to 10 Ohm.cm². However, this augmentation in series resistance led to a leftward shift in the J-V curve, subsequently causing a continual decline in the fill factor (FF) of the element. As evident in Fig. 9 (a), this shift reduced the PCE of the cell from 26.35 % to 21.81 %.

In contrast, when we enhanced the shunt resistance, scaling it up from 1000 Ohm.cm² to 10000 Ohm.cm², the PCE of the cell improved, rising from its original 25.48 %-26.73 %. This enhancement can be attributed to the fact that a higher shunt resistance minimizes power consumption and leakage. As the shunt resistance increased from 1000 Ohm.cm² to 10000 Ohm.cm², the photoelectric conversion efficiency continued to exhibit an upward trend.

To enhance each material within the solar cell, various materials are tested on the back electrodes of the mentioned PSCs. This is done to determine whether other back electrodes with properties similar to Pt could be used effectively. Fig. 10 displays the photovoltaic properties of the simulated cell with a range of back electrodes, including Cu (4.65 eV), Ag (4.26 eV), C(5 eV), Au(5.1 eV), Ni(5.5 eV), and Pt(5.65 eV).

The FF in Fig. 10(b) initially exhibits an increase followed by a decrease, potentially attributed to two complementary mechanisms. Firstly, as the bandgap of the back electrode widens, it reduces carrier recombination at the interfaces and enhances carrier collection efficiency, leading to an increase in FF. However, as the bandgap increases

Table 3
Comparison of the performance of several new solar cells.

References	Voc (V)	Jsc(mA/cm ²)	FF (%)	PCE (%)	Structure Type	Material Type
[44]	1.10	16.589	85.76	15.68	p-i-n	Pb-free
[45]	1.00	25.75	79.21	20.58	n-i-p	Pb-based
[46]	0.95	29.05	81.10	22.40	n-i-p	Pb-free
[47]	1.09	27.67	85.77	26.83	n-i-p	Pb-free
This work	1.30	23.39	88.19	26.85	n-i-p	Pb-free

further, an excessively high bandgap may elevate the energy barrier for carrier injection into the electrode, hindering carrier injection and diminishing the efficiency of current generation [43]. The interplay between these factors results in a decline in FF.

After optimizing the device, we have acquired the J-V curve and QE curve as depicted in Fig. 11(a) and (b). The outcomes reveal a broadened spectral range of light absorption, extending from 300-684 nm to 300-786 nm. Following optimization, the PSC exhibits an improved Voc of 1.30 V, a Jsc of 23.39 mA/cm², a FF of 88.19 %, and ultimately, a PCE of 26.85 %.

Table 3 lists the photovoltaic parameters of some Pb-free PSCs in recent years and compares them with the cell parameters mentioned in this paper. In contrast, the all-Ge-based double-layer PSC designed in this paper provides the best overall results with the highest PCE while prioritizing material safety.

4. Conclusion

In this work, organic-inorganic hybrid Pb-free $MgAl_3\text{-}CsGeI_3$ double absorber layer PSCs with an n-i-p planar structure have been simulated. The thickness of HTL and ETL are discussed, and the thickness and

defects of the absorber layer are optimised. The performances of the PSCs are also investigated with respect to the effect of operating temperature, different resistances and back electrodes. Within the visible region, the optimised device exhibits a PCE of 26.85 %, FF of 88.19 %, J_{sc} of 23.39 mA/cm², Voc of 1.30 V, and QE of 99.8 %. This work can provide a theoretical groundwork for the design and application of Pb-free and non-toxic Ge-based double-junction solar cells in the future. Contemporary research on perovskite solar cells has significantly improved PCE. However, the enduring stability of perovskite materials poses significant challenges, hindering the widespread adoption and commercial feasibility of these devices.

CRediT authorship contribution statement

Lijing Su: Writing – original draft, Visualization, Software, Methodology, Conceptualization. **Pengfei Sun:** Formal analysis, Conceptualization. **Yixin Zhou:** Supervision, Conceptualization. **Xin Li:** Formal analysis, Conceptualization. **Sihan Nie:** Methodology. **Yang Gao:** Writing – review & editing, Supervision, Resources, Conceptualization.

Declaration of competing interest

The authors declare that they have no known competing financial interests or personal relationships that could have appeared to influence the work reported in this paper.

Data availability

Data will be made available on request.

Acknowledgements

This research was funded by the Fundamental Scientific Research Business Expense for Higher School of Heilongjiang Province(2022-KYYWF-1087).

References

- [1] Y. Cao, Q. Li, J. Zhou, et al., Boosting conversion efficiency by bandgap engineering of ecofriendly antimony trisulfide indoor photovoltaics via a modeling approach, *Sol. Energy Mater. Sol. Cell.* 273 (2024) 112961.
- [2] Y. Cao, P. Qu, C. Wang, et al., Epitaxial growth of vertically aligned antimony selenide nanorod arrays for heterostructure based self-powered photodetector, *Adv. Opt. Mater.* 10 (19) (2022) 2200816.
- [3] Y. Li, S. Huang, S. Peng, et al., Toward smart sensing by MXene, *Small* 19 (14) (2023) 2206126.
- [4] J. Zhou, J. Zhu, W. He, et al., Selective preferred orientation for high-performance antimony selenide thin-film solar cells via substrate surface modulation, *J. Alloys Compd.* 938 (2023) 168593.
- [5] Y. Cao, C. Liu, T. Yang, et al., Gradient bandgap modification for highly efficient carrier transport in antimony sulfide-selenide tandem solar cells, *Sol. Energy Mater. Sol. Cell.* 246 (2022) 111926.
- [6] A. Kojima, K. Teshima, Y. Shirai, et al., Organometal halide perovskites as visible-light sensitizers for photovoltaic cells, *J. Am. Chem. Soc.* 131 (17) (2009) 6050–6051.
- [7] Y. Chen, L. Zhang, Y. Zhang, et al., Large-area perovskite solar cells-a review of recent progress and issues, *RSC Adv.* 8 (19) (2018) 10489–10508.
- [8] Q. Zhang, W. Zhu, D. Chen, et al., Light processing enables efficient carbon-based, all-inorganic planar CsPbI₂ solar cells with high photovoltages, *ACS Appl. Mater. Interfaces* 11 (3) (2018) 2997–3005.
- [9] S. Liu, V.P. Biju, Y. Qi, et al., Recent progress in the development of high-efficiency inverted perovskite solar cells, *NPG Asia Mater.* 15 (1) (2023) 27.
- [10] A.S.R. Bati, Y.L. Zhong, P.L. Burn, et al., Next-generation applications for integrated perovskite solar cells, *Commun. Mater.* 4 (1) (2023) 2.
- [11] J. Thiesbrummel, S. Shah, E. Gutierrez-Partida, et al., Ion-induced field screening as a dominant factor in perovskite solar cell operational stability, *Nat. Energy* (2024) 1–13.
- [12] J. Huang, Y. Yuan, Y. Shao, et al., Understanding the physical properties of hybrid perovskites for photovoltaic applications, *Nat. Rev. Mater.* 2 (7) (2017) 1–19.
- [13] M. Salado, R.K. Kokal, L. Calio, et al., Identifying the charge generation dynamics in Cs⁺-based triple cation mixed perovskite solar cells, *Phys. Chem. Chem. Phys.* 19 (34) (2017) 22905–22914.
- [14] S. Kazim, F.J. Ramos, P. Gao, et al., A dopant free linear acene derivative as a hole transport material for perovskite pigmented solar cells, *Energy Environ. Sci.* 8 (6) (2015) 1816–1823.
- [15] N. Kaur, R. Pandey, J. Madan, Machine learning-driven exploration of cesium-based all-inorganic mixed-halide perovskite solar cells with a double absorber layer architecture, *J. Electron. Mater.* 53 (9) (2024) 5361–5373.
- [16] J. Cao, F. Yan, Recent progress in tin-based perovskite solar cells, *Energy Environ. Sci.* 14 (3) (2021) 1286–1325.
- [17] K.P. Marshall, M. Walker, R.I. Walton, et al., Enhanced stability and efficiency in hole-transport-layer-free CsSnI₃ perovskite photovoltaics, *Nat. Energy* 1 (12) (2016) 1–9.
- [18] N.K. Noel, S.D. Stranks, A. Abate, et al., Lead-free organic-inorganic tin halide perovskites for photovoltaic applications, *Energy Environ. Sci.* 7 (9) (2014) 3061–3068.
- [19] F. Hao, C.C. Stoumpos, D.H. Cao, et al., Lead-free solid-state organic-inorganic halide perovskite solar cells, *Nat. Photonics* 8 (6) (2014) 489–494.
- [20] A. Hima, N. Lakhdar, Enhancement of efficiency and stability of CH₃NH₃GeI₃ solar cells with CuSbS₂, *Opt. Mater.* 99 (2020) 109607.
- [21] X. Chang, D. Marongiu, V. Sarritzu, et al., Layered germanium hybrid perovskite bromides: insights from experiments and first-principles calculations, *Adv. Funct. Mater.* 29 (31) (2019) 1903528.
- [22] T. Krishnamoorthy, H. Ding, C. Yan, et al., Lead-free germanium iodide perovskite materials for photovoltaic applications, *J. Mater. Chem. A* 3 (47) (2015) 23829–23832.
- [23] F. Behrouznejad, S. Shahbazi, N. Taghavinia, et al., A study on utilizing different metals as the back contact of CH₃NH₃PbI₃ perovskite solar cells, *J. Mater. Chem. A* 4 (35) (2016) 13488–13498.
- [24] J. Bing, J. Kim, M. Zhang, et al., The impact of a dynamic two-step solution process on film formation of Cs_{0.15}(MA_{0.7}FA_{0.3})_{0.85}PbI₃ perovskite and solar cell performance, *Small* 15 (9) (2019) 1804858.
- [25] P. Chevanathan, M.I. Hossain, N. Amin, Performance analysis of copper-indium-gallium-diselenide (CIGS) solar cells with various buffer layers by SCAPS[J], *Curr. Appl. Phys.* 10 (3) (2010) S387–S391.
- [26] D.B. Khadka, Y. Shirai, M. Yanagida, et al., Degradation of encapsulated perovskite solar cells driven by deep trap states and interfacial deterioration, *J. Mater. Chem. C* 6 (1) (2018) 162–170.
- [27] F. Liu, J. Zhu, J. Wei, et al., Numerical simulation: toward the design of high-efficiency planar perovskite solar cells, *Appl. Phys. Lett.* 104 (25) (2014).
- [28] S. Zandi, P. Saxena, N.E. Gorji, Numerical simulation of heat distribution in RGO-contacted perovskite solar cells using COMSOL, *Sol. Energy* 197 (2020) 105–110.
- [29] G. Pindolia, S.M. Shinde, P.K. Jha, Optimization of an inorganic lead free RbGeI₃ based perovskite solar cell by SCAPS-1D simulation, *Sol. Energy* 236 (2022) 802–821.
- [30] H. Son, B.S. Jeong, Optimization of the power conversion efficiency of CsPbIxBr_{3-x}-based perovskite photovoltaic solar cells using ZnO and NiOx as an inorganic charge transport layer, *Appl. Sci.* 12 (18) (2022) 8987.
- [31] J. Xu, J. Yin, L. Xiao, et al., Bromide regulated film formation of CH₃NH₃PbI₃ in low-pressure vapor-assisted deposition for efficient planar-heterojunction perovskite solar cells, *Sol. Energy Mater. Sol. Cell.* 157 (2016) 1026–1037.
- [32] X. Zhang, T. Li, Q. Wei, et al., Germanium-lead double absorber layer perovskite solar cells: further performance enhancement from the perspective of device simulation, *Opt. Commun.* 530 (2023) 129188.
- [33] J. Liu, X. Meng, K. Liu, et al., Optimizing the performance of Ge-based perovskite solar cells by doping CsGeI₃ instead of charge transport layer, *Sol. Energy* 259 (2023) 398–415.
- [34] M.H. Miah, M.B. Rahman, F. Khatun, et al., Optimization and detail analysis of novel structure Pb-free CsGeI₃-based all-inorganic perovskite solar cells by SCAPS-1D, *Optik* 281 (2023) 170819.
- [35] I. Chabri, Y. Benhouria, A. Oubelkacem, et al., Enhance stability of γ-CsSnI₃-based PSCs by (γ-CsSnI₃-Cs₂SnI₆) heterojunction, *Sol. Energy Mater. Sol. Cell.* 259 (2023) 112426.
- [36] V. Garg, A. Kumar, P. Sharma, Numerical simulation of novel lead-free Cs₃Sb₂Br₉ absorber-based highly efficient perovskite solar cell, *Opt. Mater.* 122 (2021) 111715.
- [37] S. Agarwal, P.R. Nair, Device engineering of perovskite solar cells to achieve near ideal efficiency, *Appl. Phys. Lett.* 107 (12) (2015).
- [38] Y. He, L. Xu, C. Yang, et al., Design and numerical investigation of a lead-free inorganic layered double perovskite Cs₄CuSb₂Cl₁₂ nanocrystal solar cell by SCAPS-1D, *Nanomaterials* 11 (9) (2021) 2321.
- [39] A. Zhang, R. Duan, Design and numerical investigation of CsPbI₃/CsSnO_{0.5}Ge_{0.5}I₃ double-absorption-layer heterojunction perovskite solar cells based on SCAPS-1D, *Phys. Status Solidi* 220 (21) (2023) 2300525.
- [40] Z. Ni, C. Bao, Y. Liu, et al., Resolving spatial and energetic distributions of trap states in metal halide perovskite solar cells, *Science* 367 (6484) (2020) 1352–1358.
- [41] A. Tara, V. Bharti, S. Sharma, et al., Computational approach to explore suitable charge transport layers for all inorganic CsGeI₃ perovskite solar cells, *Opt. Mater.* 128 (2022) 112403.
- [42] I. Chabri, A. Oubelkacem, Y. Benhouria, et al., Performance optimization of a CsGeI₃-based solar device by numerical simulation, *Mater. Sci. Eng., B* 297 (2023) 116757.
- [43] R. Chen, W. Zhang, X. Guan, et al., Rear electrode materials for perovskite solar cells, *Adv. Funct. Mater.* 32 (26) (2022) 2200651.
- [44] S.S. Nair, P. Thakur, F. Wan, et al., Performance evaluation and the optimization of an inverted photo voltaic cell with lead-free double perovskite material and inorganic transport layer materials, *Sol. Energy* 262 (2023) 111823.

- [45] M.S.I. Sadek, M.S. Aktar, M.F.K. Shimul, et al., Performance analysis of perovskite solar cells with all inorganic hole transport and electron transport layers, *J. Eng. Stud. Res.* 1 (1) (2021) 25–30.
- [46] A. Alsalme, H. Alsaeedi, Twenty-two percent efficient Pb-free all-perovskite tandem solar cells using SCAPS-1D, *Nanomaterials* 13 (1) (2022) 96.
- [47] Y. Fan, X. Meng, X. Liu, et al., Performance optimization of all-inorganic CsGel3 solar cells: SCAPS simulation and DFT calculation, *Chem. Phys. Lett.* 830 (2023) 140809.